

NADPH production by the oxidative pentose-phosphate pathway supports folate metabolism

Li Chen^{1,2}, Zhaoyue Zhang^{1,2}, Atsushi Hoshino³, Henry D. Zheng^{1,2}, Michael Morley³, Zoltan Arany³ and Joshua D. Rabinowitz^{1,2*}

NADPH donates high-energy electrons for antioxidant defence and reductive biosynthesis. Cytosolic NADP is recycled to NADPH by the oxidative pentose-phosphate pathway (oxPPP), malic enzyme 1 (ME1) and isocitrate dehydrogenase 1 (IDH1). Here we show that any one of these routes can support cell growth, but the oxPPP is uniquely required to maintain a normal NADPH/NADP ratio, mammalian dihydrofolate reductase (DHFR) activity and folate metabolism. These findings are based on CRISPR deletions of glucose-6-phosphate dehydrogenase (G6PD, the committed oxPPP enzyme), ME1, IDH1 and combinations thereof in HCT116 colon cancer cells. Loss of G6PD results in high NADP, which induces compensatory increases in ME1 and IDH1 flux. But the high NADP inhibits DHFR, resulting in impaired folate-mediated biosynthesis, which is reversed by recombinant expression of *Escherichia coli* DHFR. Across different cancer cell lines, G6PD deletion produced consistent changes in folate-related metabolites, suggesting a general requirement for the oxPPP to support folate metabolism.

The cofactor NADPH provides high-energy electrons for antioxidant defence and reductive biosynthesis. Consumption and production of NADPH is compartmentalized, with cytosolic NADPH used by enzymes including fatty acid synthase, ribonucleotide reductase, thioredoxin reductase and glutathione reductase^{1,2}. Regeneration of cytosolic NADPH from NADP occurs by three well-validated routes: ME1, IDH1 and the oxPPP, in which NADPH is produced by both G6PD and 6-phosphogluconate dehydrogenase (PGD) (Fig. 1a)^{3,4}. Each of these enzymes is ubiquitously expressed across mammalian cells and tissues.

G6PD is the best studied, largely because G6PD deficiency is the most common human enzyme defect⁵. Hypomorphic alleles of G6PD result in protection from malaria at the expense of red blood cell sensitivity to oxidative stressors⁶. Except in red blood cells, which are unique in lacking mitochondria, hypomorphic alleles of G6PD are well tolerated, suggesting that adequate oxPPP flux is maintained despite the partially defective enzyme, or that other NADPH production pathways can compensate for the decreased oxPPP. In mice, homozygous deletion of G6PD but not IDH1 or ME1 is embryonic lethal^{7–9}.

To explore the physiological activity of metabolic enzymes, a classical approach is tracing using isotope-labelled carbon (¹³C or ¹⁴C)^{10–12}. This approach has limited utility for ME1 and IDH1, as the same carbon transformation can be carried out by other isozymes that do not make NADPH. An alternative approach uses deuterium (²H) to probe more directly the source of NADPH's redox-active hydrogen^{13,14}. Deuterium-tracing studies suggest that, in most cultured mammalian cells, the oxPPP is the largest cytosolic NADPH producer^{1,15}. But exceptions exist. For example, ME1 plays the largest role in differentiating adipocytes¹⁴. Moreover, deuterium tracing is complicated by the potential for loss of the ²H tracer via hydrogen–deuterium exchange and the deuterium kinetic isotope effect of many NADPH-producing enzymes (the greater mass of deuterium resulting in the reaction occurring more slowly with labelled substrate)¹⁶. In addition, some estimates of cytosolic NADPH demand

for fatty acid, proline and deoxyribonucleotide synthesis and redox defence have exceeded measurements of the combined production by the oxPPP, IDH1 and ME1¹³. Due to these issues, it remains unclear whether cytosolic NADPH production in most cell types is fully accounted for by the oxPPP, IDH1 and ME1, or whether other NADPH production routes are also important.

One potential alternative NADPH source is folate metabolism¹³. The canonical function of folate metabolism is to provide activated one-carbon units to enable synthesis of thymidine, purines and methionine^{17–20}. The one-carbon carrier tetrahydrofolate (THF) is made from dihydrofolate (DHF) by the enzyme DHFR. THF is then loaded with a one-carbon unit, usually from serine, to make methylene-THF. Oxidation of this one-carbon unit can make NADPH via two different reactions: (i) production of formyl-THF, a key substrate for purine synthesis, from methylene-THF, and (ii) oxidation of formyl-THF's one-carbon unit to CO₂. In most cell types, folate metabolism does not make substantial cytosolic NADPH, although it can contribute substantially to mitochondrial NADPH via formyl-THF oxidation^{1,21,22}.

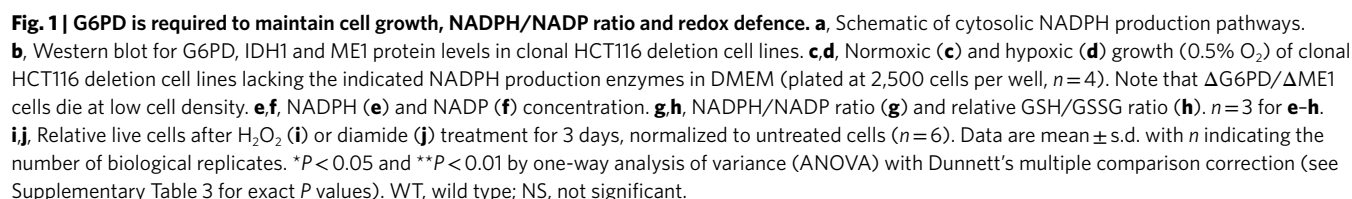
Here we systematically genetically dissect cytosolic NADPH sources. We find that cancer cells can tolerate loss of any two of the three canonical cytosolic NADPH production routes. Among these, loss of the oxPPP due to G6PD knockout is most impactful, resulting in decreased NADPH/NADP ratio, oxidative stress sensitivity and slow growth. Strikingly, the strongest metabolic effect of G6PD knockout does not relate to any of the canonical NADPH products, such as fatty acids or glutathione. Instead, we observed profound defects in folate metabolism. These arise from impaired DHFR activity and are overcome by engineered expression of *E. coli*, reflecting a requirement for the oxPPP to maintain mammalian DHFR flux.

Results

G6PD is necessary and sufficient to maintain cytosolic NADPH/NADP homeostasis. To probe the importance of different cytosolic

¹Department of Chemistry, Princeton University, Princeton, NJ, USA. ²Lewis-Sigler Institute for Integrative Genomics, Princeton University, Princeton, NJ, USA. ³Department of Medicine and Cardiovascular Institute, Perelman School of Medicine, University of Pennsylvania, Philadelphia, PA, USA.

*e-mail: josh@princeton.edu



NADP and NADPH were measured in the resulting single- and double-deletion cell lines using liquid chromatography–mass spectrometry (LC–MS). NADPH concentration was maintained in all of the cell lines (Fig. 1e). NADP, however, rose in the Δ G6PD cells (but none of the other single deletions, including PGD), and more

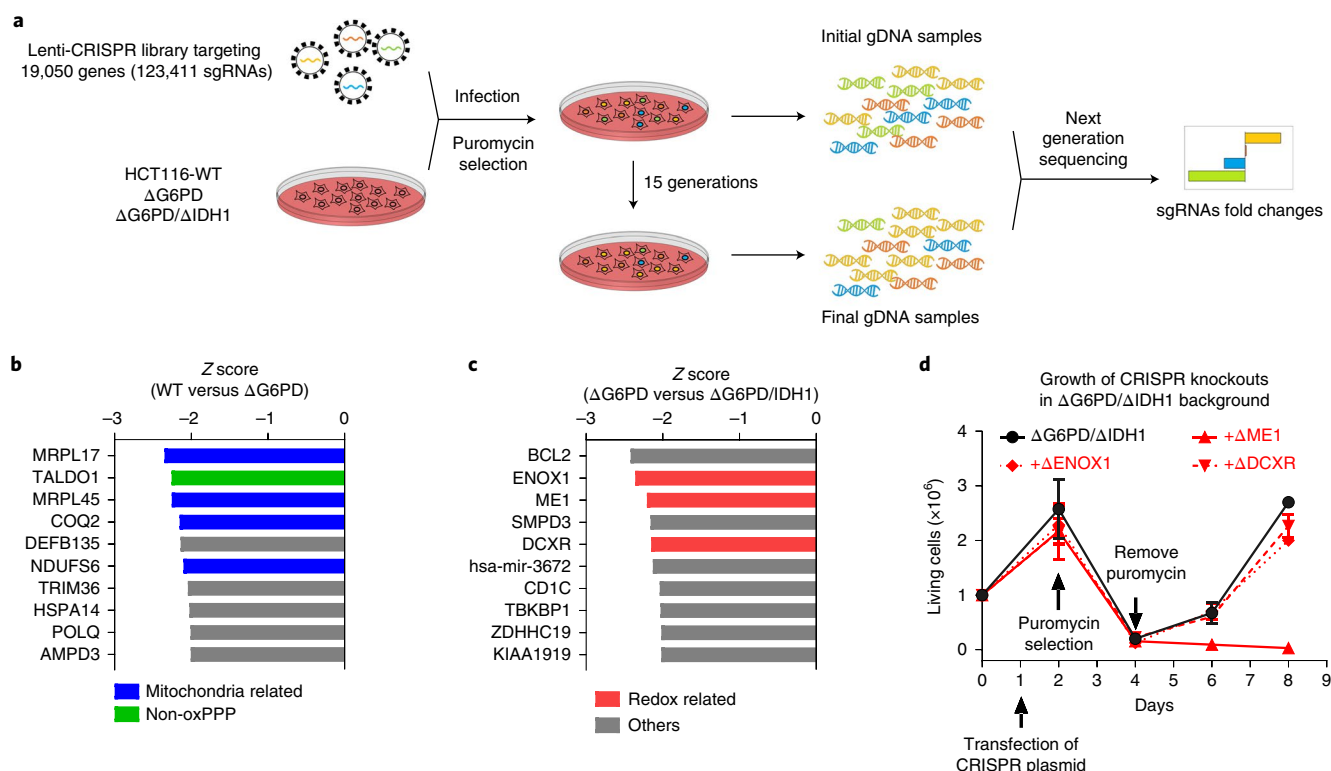


Fig. 2 | CRISPR-based genetic screen identifies no cytosolic NADPH producers beyond oxPPP, ME1 and IDH1. **a**, Schematic of the screen, which is based on comparing gene essentiality both in WT versus Δ G6PD knockout cells and in Δ G6PD versus Δ G6PD/ Δ IDH1 knockout cells. gDNA, genomic DNA. **b**, Top ten conditional essential genes in Δ G6PD compared with WT HCT116 cells on the basis of Z score. **c**, Top ten conditional essential genes in Δ G6PD/ Δ IDH1 compared with Δ G6PD cells on the basis of Z score. **d**, Cell growth of targeted pooled CRISPR knockout of DCXR, ENOX1 or ME1 in the Δ G6PD/ Δ IDH1 background (mean \pm s.d., $n = 4$). After puromycin selection of transfected cells, only ME1, but not the other tested screen hits, was validated in the targeted knockout experiments.

profoundly in the Δ G6PD/ Δ ME1 cells (Fig. 1f and Supplementary Fig. 1d). The decreased NADPH/NADP ratio (Fig. 1g) resulted in more oxidized glutathione and thus a decreased reduced/oxidized glutathione ratio in Δ G6PD/ Δ IDH1 and Δ G6PD/ Δ ME1 cells (Fig. 1h and Supplementary Fig. 1e). All of the lines lacking G6PD were more sensitive to diamide and H_2O_2 (Fig. 1i,j). Both IDH1 and G6PD knockout cells, but not ME1 knockout cells, showed defective growth in a hypoxic environment, although the defect associated with G6PD loss was more severe (Fig. 1d). In the hypoxic G6PD knockout cells, addition of glutathione or *N*-acetyl cysteine mitigated these defects (Supplementary Fig. 1f). Overall, these findings are consistent with the G6PD-deficient cells having impaired growth and oxidative defence because they fail to maintain a high NADPH/NADP ratio.

The oxPPP, ME1 and IDH1 are the only major cytosolic NADPH producers. Previous studies have yielded conflicting evidence as to whether there are substantial contributors to cytosolic NADPH production beyond the oxPPP, IDH1 and ME1 (refs. 1,13,15). We previously proposed that folate metabolism could potentially produce both cytosolic and mitochondrial NADPH¹³, although subsequent research showed that such production is typically limited to the mitochondrion, except in mitochondrial folate pathway mutants²¹. Using [3H]serine to trace folate-dependent NADPH production, we confirmed minimal contribution in HCT116 cells (Supplementary Fig. 2a). To explore the possibility of other cytosolic NADPH production routes, we first attempted to make triple deletion Δ G6PD/ Δ IDH1/ Δ ME1 cells by knocking out IDH1 (whose loss is well tolerated in both wild-type and Δ G6PD cells) in Δ G6PD/ Δ ME1 cells. Although we did obtain a single-cell line with heterozygous loss of

one copy of IDH1, repeated efforts using CRISPR, puromycin selection and single-cell cloning never resulted in viable Δ G6PD/ Δ ME1/ Δ IDH1 cells. Thus, HCT116 cells require at least one of the three major known cytosolic NADPH production routes.

Despite not being sufficient on their own to support cell growth, other enzymes may contribute to HCT116's cytosolic NADPH production. To search for potential unknown enzymes that might contribute to cytosolic NADPH homeostasis, we carried out a genome-scale CRISPR deletion screen for genes that are conditionally essential on loss of G6PD or both G6PD and IDH1. This was done by infecting Δ G6PD cells or Δ G6PD/ Δ IDH1 cells with GeCKOv2 lentiCRISPR library. After selection with puromycin, we allowed cells to passage for 15 doublings and collected genomic DNAs from the first and last generations of cells for sequencing (Fig. 2a). A challenge in such screens is the potential for clonal effects (genes that are conditionally essential in a particular single-cell clone, irrespective of the G6PD/ Δ IDH1 status). To address this, the screen was conducted in two independent Δ G6PD cell lines and two independent Δ G6PD/ Δ IDH1 cell lines (Supplementary Fig. 2b–d). In the Δ G6PD background, a top hit was TALDO1 (Fig. 2b), a logical outcome given that the loss of the oxPPP should render the non-oxidative pentose-phosphate pathway essential for ribose production. Several mitochondria-related genes were also hits, suggesting that G6PD loss sensitizes to mitochondrial dysfunction (Fig. 2b). The screen did not yield any hits related to cytosolic NADPH.

In the Δ G6PD/ Δ IDH1 background, the top three overall hits were BCL2, ENOX1 and ME1 (Fig. 2c). Thus, the screen effectively identified ME1 as being essential in cells already lacking G6PD and IDH1. BCL2 is presumably essential for preventing apoptosis in cells stressed by G6PD and IDH1 loss. ENOX1 encodes an enzyme

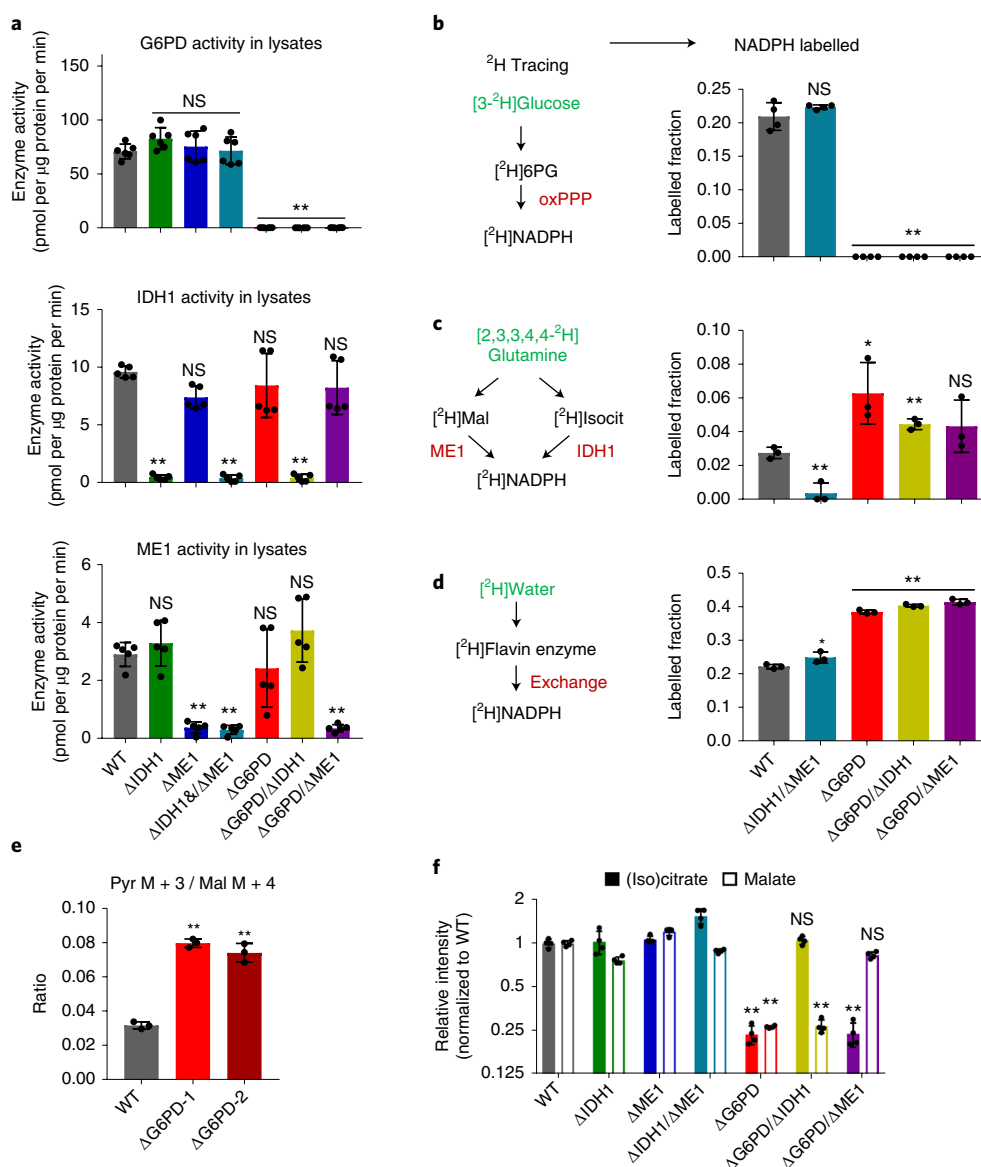


Fig. 3 | Loss of G6PD induces ME1 and IDH1 flux without altering their enzyme activities. **a**, Enzyme activity of G6PD (top), IDH1 (middle) and ME1 (bottom) in clonal HCT116 deletion cell lysates ($n = 6$). **b**, Labelling of NADPH's redox-active hydrogen in cells fed $[3-^2\text{H}]\text{glucose}$ to trace NADPH production from oxPPP ($n = 3$). **c**, Labelling of NADPH's redox-active hydrogen in cells fed $[2,3,3,4,4-^2\text{H}]\text{glutamine}$ to trace NADPH production from ME1 and/or IDH1, which are not differentiated by this tracer ($n = 3$). **d**, Labelling of NADPH's redox-active hydrogen in HCT116 mutants cultured in 45% D_2O to trace H-D exchange of redox-active hydrogen nucleus (but not high-energy electrons) of NADPH with water ($n = 3$). **e**, Ratio of pyruvate M + 3/malate M + 4 from $[\text{U}-^{13}\text{C}]\text{glutamine}$, reflecting the ratio of malic enzyme flux to glycolysis flux ($n = 3$). **f**, Relative malate and (iso)citrate levels in NADPH gene deletion cell lines ($n = 4$). Data are mean \pm s.d. with n indicating the number of biological replicates. * $P < 0.05$ and ** $P < 0.01$ by one-way ANOVA with Dunnett's multiple comparison correction (see Supplementary Table 3 for exact P values).

involved in NAD(P)H oxidation at the plasma membrane, which appears to play a role in angiogenesis and protection of cancer from radiotherapy. Another top-ten hit was the DCXR gene, which encodes an NADPH-consuming xylulose reductase that makes the osmolyte xylitol in renal tubules. While ENOX1 and DCXR are annotated to consume, not make, NAD(P)H, we were curious if they might act in reverse to contribute to NADPH homeostasis in Δ G6PD/ Δ IDH1 cells. In an effort to validate their importance for growth in the absence of G6PD and IDH1, we performed directed knockout of these two genes, as well as ME1, in Δ G6PD/ Δ IDH1 cells (Fig. 2d). Successful knockout was validated by sequencing (Supplementary Fig. 2e). Loss of ENOX1 and DCXR were tolerated, whereas loss of ME1 was not (Fig. 2d). Thus, HCT116 cells require

at least one of G6PD, IDH1 and ME1 to grow. Our failure to identify other NADPH producers in these genome-scale screens (or genes of unknown function that turned out to be NADPH producers) supports the perspective that HCT116 cells rely solely on G6PD, IDH1 and ME1 for cytosolic NADPH production.

Increased ME1 and IDH1 flux compensates for loss of G6PD.

Having confirmed the absence of other substantial cytosolic NADPH producers, we investigated the mechanism by which loss of any two of the three major producers can be compensated. Western blots of lysates from single- and double-deletion cells showed clean knockout patterns consistent with their genetic background, but no compensatory expression of the remaining enzyme(s) (Fig. 1b).

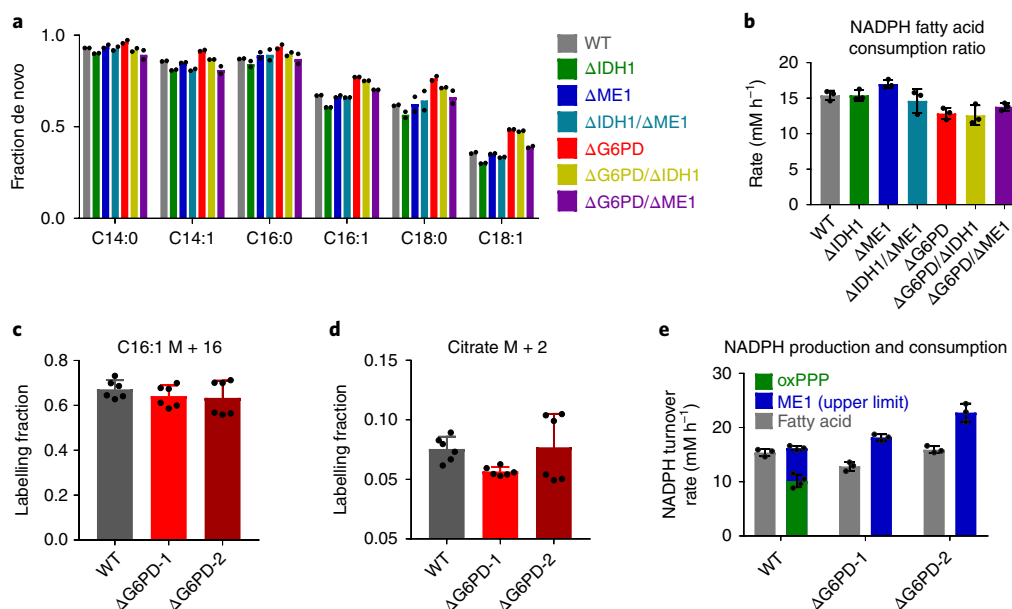


Fig. 4 | Fatty acid synthesis is maintained in HCT116 G6PD knockout cells. **a**, Fraction of different non-essential fatty acid species synthesized de novo on the basis of extent of labelling from $[U-^{13}C]$ glucose (for full labelling patterns, see Supplementary Fig. 3, $n = 2$). **b**, NADPH consumption for fatty acid synthesis ($n = 3$). **c,d**, Palmitoleic acid (C16:1) (**c**) and citrate labelling (**d**) in cells fed $100 \mu M$ $[U-^{13}C]$ palmitate (conjugated to BSA) for 24 h ($n = 6$). **e**, NADPH production by the oxPPP (measured using ^{14}C -CO₂ release from $[1-^{14}C]$ and $[6-^{14}C]$ glucose, $n = 4$) and the upper limit of production by ME1 (measured on the basis of $[U-^{13}C]$ lactate production from $[U-^{13}C]$ glutamine, $n = 3$) and NADPH consumption flux for fatty acid synthesis ($n = 3$). Data are mean \pm s.d. with n indicating the number of biological replicates.

Similarly, enzymatic assays in cytosolic lysates revealed expected knockout patterns without compensatory upregulation of other NADPH enzyme activities (Fig. 3a). Thus, there is no compensation for loss of G6PD, ME1 or IDH1 by enzyme induction.

Even if enzyme levels and in vitro activities remain the same, fluxes may differ due to changes in substrate, product and effector levels in cells. To probe NADPH production fluxes, we used deuterated tracers. $[3-^2H]$ Glucose labels the redox-active hydrogen of NADPH at the PGD step of the oxPPP. As expected, this labelling is abolished by G6PD deletion (Fig. 3b). The labelling did not change with deletion of IDH1 and ME1, consistent with oxPPP flux exceeding IDH1 and ME1 flux even before loss of these enzymes. $[2,3,3,4,4-^2H]$ Glutamine labels malate and isocitrate, and thereby can label NADPH via ME1 and IDH1. We observed NADPH redox-active hydrogen labelling from $[2,3,3,4,4-^2H]$ glutamine in wild-type cells, which is lost with deletion of both ME1 and IDH1. Labelling increased with deletion of G6PD (Fig. 3c). These tracer studies show that, in HCT116 cells, the oxPPP is the default cytosolic NADPH production pathway. When this pathway is eliminated, IDH1 and ME1 compensate for G6PD loss.

The extent of NADPH active hydrogen labelling is far from complete in either $[3-^2H]$ glucose or $[2,3,3,4,4-^2H]$ glutamine. We recently discovered that a major source of NADPH's redox-active hydrogen nucleus (but not its high-energy electrons) is H–D exchange with water¹⁵. This exchange occurs when NADPH's redox-active hydrogen, normally held in a stable C–H bond, is transferred reversibly to a flavin cofactor. The flavin cofactor holds the redox-active hydrogen in an N–H bond that quickly trades the hydrogen nucleus back and forth with water. The net effect is dilution of labelling from substrates such as $[3-^2H]$ glucose and $[2,3,3,4,4-^2H]$ glutamine. To quantify such exchange, we used 2H -labelled water as a tracer. This exchange was not altered by ME1 and IDH1 deletion, but increased substantially with G6PD loss. The increased NADPH labelling from deuterated water on G6PD knockout is consistent with increased NADP leading to greater flavin enzyme reversibility: more NADP is

available to accept flavin's redox-active hydrogen, which is labelled from the added D₂O. Taking into consideration the extent of H–D exchange (see Methods), labelling from $[3-^2H]$ glucose is consistent with the oxPPP accounting for most of NADPH in wild-type HCT116 cells, and from $[2,3,3,4,4-^2H]$ glutamine is consistent with malic enzyme and IDH together accounting for most of NADPH in Δ G6PD cells.

As further confirmation of the increased malic enzyme flux in Δ G6PD cells, we employed $[U-^{13}C]$ glutamine tracer. Catabolism of $[U-^{13}C]$ glutamine generates $[U-^{13}C]$ malate. Malic enzyme activity can then generate $[U-^{13}C]$ pyruvate, with the fraction of $[U-^{13}C]$ pyruvate, normalized to the fraction of $[U-^{13}C]$ malate, indicative of the relative flux of malic enzyme compared with glycolysis. These ^{13}C -based measurements track total malic enzyme activity, without regard to the isozyme, compartment or cofactor involved. Using this approach, we observed a twofold increase in total malic enzyme activity in the Δ G6PD clones (Fig. 3e).

Increased ME1 and IDH1 flux might manifest as decreased concentrations of the enzymes' substrates, malate and isocitrate. Citrate and isocitrate are isomers that are connected by the reversible aconitase reaction and are not readily distinguished by LC–MS. Strikingly, in G6PD knockout cells, we observed a fourfold decrease in the intracellular concentrations of both (iso)citrate and malate (Fig. 3f). These concentration changes reflected increased consumption by ME1 and IDH1: malate depletion was reversed by ME1 knockout, and (iso)citrate depletion was reversed by IDH1 knockout. Thus, G6PD knockout triggers, probably through increased NADP rather than altered enzyme activities, sufficiently enhanced flux through ME1 and IDH1 so as to deplete cellular malate and citrate.

Fatty acid biosynthesis is maintained in G6PD knockout cells. In addition to turning on ME1 and IDH1, another way of coping with G6PD loss would be to decrease NADPH demand. Two major uses of NADPH in growing cultured cancer cells

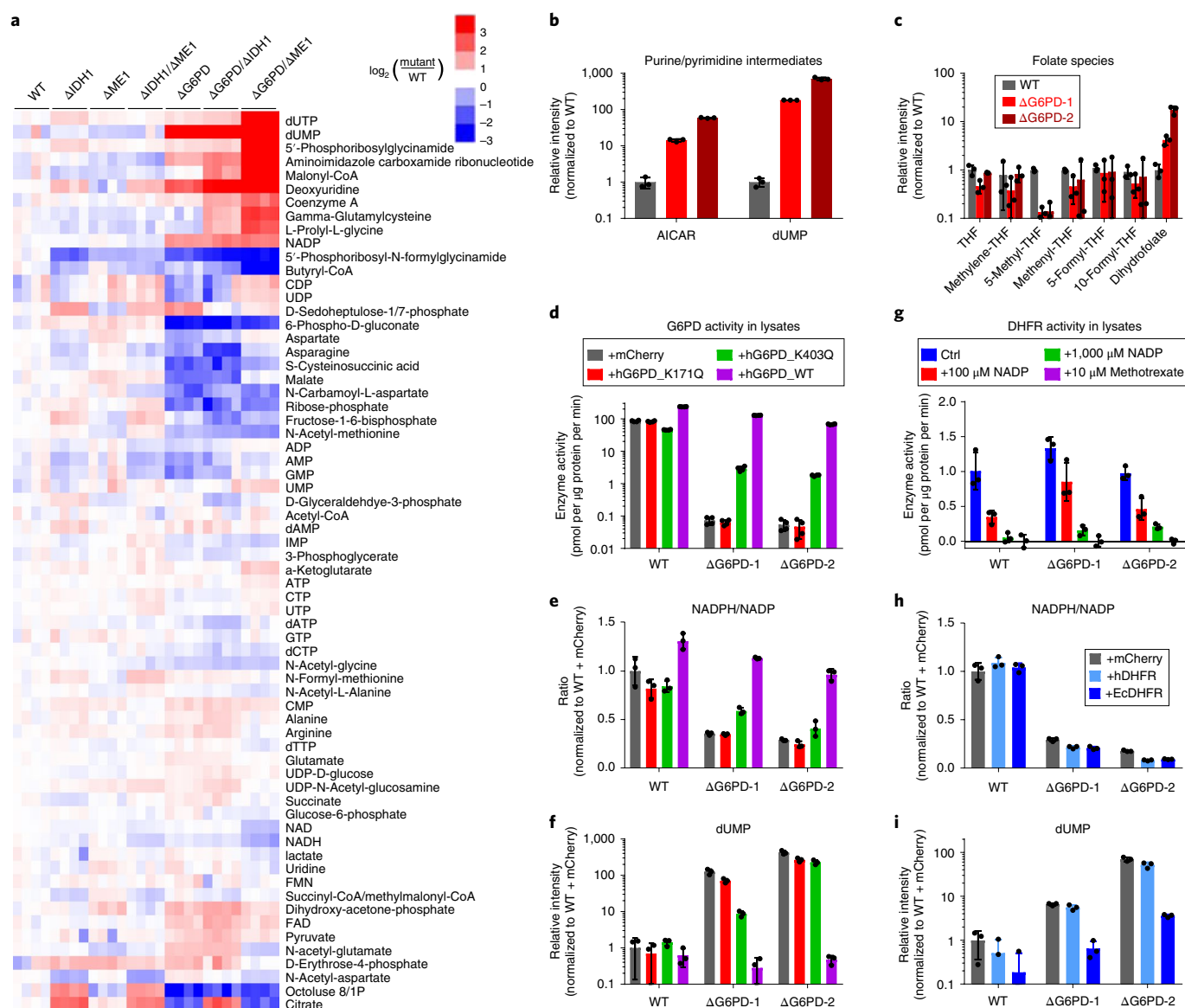


Fig. 5 | G6PD knockout cells are defective in folate metabolism due to impaired DHFR activity. **a**, Heat map showing intracellular levels of water-soluble metabolites in clonal HCT116 deletion cell lines. For each cell line, four individual biological replicates are shown, normalized to WT cells. **b**, Relative levels of 1C-related purine/pyrimidine intermediates in ΔG6PD cells. **c**, Relative levels of folate species in ΔG6PD cells. **d–f**, G6PD activity (**d**), relative NADPH/NADP ratio (**e**) and dUMP levels (**f**) in ΔG6PD cells with doxycycline-induced expression of mCherry control or catalytically inactive (K171Q), impaired (K403Q) or WT human G6PD. **g**, DHFR enzyme activity in lysates from WT and ΔG6PD cells and its inhibition by NADP. **h,i**, Relative NADPH/NADP ratio (**h**) and dUMP levels (**i**) in ΔG6PD cells with doxycycline-induced expression of mCherry control or human DHFR or *E. coli* DHFR. All results are mean ± s.d. with *n* = 3 biological replicates.

are deoxyribonucleotide synthesis and fatty acid synthesis. Deoxyribonucleotide synthesis is essential for cell growth. Fatty acid synthesis, however, can be decreased by scavenging serum fatty acids from the media or decreasing fatty acid oxidation flux. To measure fatty acid synthesis, we fed the various knockout cell lines [$U\text{-}^{13}\text{C}$]glucose and monitored the extent of fatty acid labelling. De novo fatty acid synthesis can be distinguished from scavenging of serum fat by ^{13}C incorporation. The fraction of fatty acids containing multiple ^{13}C atoms, indicative of de novo synthesis, was similar across cell lines lacking different cytosolic NADPH-producing enzymes (Fig. 4a and Supplementary Fig. 3). Moreover, the NADPH consumption to support fatty acid synthesis, calculated on the basis of the abundances and extent of labelling of the different major fatty acid species, was also similar (Fig. 4b). To examine fatty acid oxidation in G6PD knockout cells, we fed cells [$U\text{-}^{13}\text{C}$]palmitate

(conjugated to bovine serum albumin). Both wild-type and knockout cells similarly assimilated the added labelled palmitate (C16:0) into palmitoleic acid (C16:1), indicating effective penetration of the tracer into both cell types (Fig. 4c). Moreover, in both cell types, labelling of tricarboxylic acid (TCA) intermediates was similar, suggesting a similar rate of fatty acid oxidation (Fig. 4d). On the basis of the similar accumulation of de novo-synthesized fatty acids from labelled glucose, and similar fatty acid oxidation rate, we conclude that NADPH usage for fatty acid synthesis is largely maintained in the G6PD knockout cells.

We were curious if the malic enzyme flux is sufficient to support this maintained rate of fatty acid synthesis. To this end, we used ^{13}C -based measurements of malic enzyme flux. While not ME1 specific, total malic enzyme flux can be determined by comparing the fraction of pyruvate made by malic enzyme with pyruvate

made via glycolysis, with the absolute glycolytic flux measured on the basis of lactate secretion rate. We observed a basal malic enzyme flux of 6 mMh^{-1} , which increased by $12\text{--}14 \text{ mMh}^{-1}$ in two separate ΔG6PD clones. This increase is similar to the absolute NADPH production flux of the oxPPP in wild-type cells, as measured by $^{14}\text{CO}_2$ release from $[1\text{-}^{14}\text{C}]\text{glucose}$ versus $[6\text{-}^{14}\text{C}]\text{glucose}$ (10 mMh^{-1}). These values can also be compared with the absolute NADPH flux required to support de novo fatty acid synthesis, as measured by the $[\text{U-}^{13}\text{C}]\text{glucose}$ labelling experiment, of $12\text{--}15 \text{ mMh}^{-1}$ (Fig. 4e). Thus, increased flux through malic enzyme is sufficient to compensate for G6PD loss without compromising NADPH-dependent biosynthesis. The malic enzyme flux is driven by NADP accumulation. Accordingly, while NADPH production flux is maintained, the NADPH/NADP ratio is not.

Untargeted metabolomics of G6PD knockout cells reveals altered folate metabolism. To search for additional consequences of impaired cytosolic NADPH production, we next conducted untargeted metabolomics in the various HCT116 single- and double-deletion cell lines (Fig. 5a). G6PD deletion resulted in a stronger and broader change in the metabolome than either IDH1 or ME1 deletion. With a few exceptions, such as citrate being higher selectively in IDH1 knockout cells, similar direction of change was observed across the different cell lines lacking G6PD. Several of these changes were expected, such as strong depletion of 6-phosphogluconate, ribose phosphate and octulose phosphate (which is made from ribose phosphate by aldolase). Substantial accumulation occurred for malonyl-CoA, especially in the cells lacking both G6PD and ME1, consistent with impairment of the reductive steps of fatty acid synthesis and thus buildup of the upstream substrate, which pushes the pathway forward.

In addition to these changes that related to known roles of the pentose-phosphate pathway, we observed striking changes in a set of metabolites related to one-carbon metabolism. The two main products of one-carbon metabolism in cell culture are purines and thymidine. Thymidylate synthase methylates dUMP using methylene-THF as the one-carbon donor. Although levels of the direct DNA precursor dTTP were maintained, we observed marked accumulation of dUMP, as well as its phosphorylated and dephosphorylated derivatives (dUTP, deoxyuridine) (Fig. 5a,b).

Purine biosynthesis involves two different reactions that consume formyl-THF. While purine end-product levels were maintained, we observed strong accumulation of the substrates of both of the formyl-THF consuming reactions: 5'-phosphoribosylglycinamide (GAR) and 5-aminoimidazole-4-carboxamide ribonucleotide (AICAR) (Fig. 5a,b). In addition, the product of the first of these reactions, 5'-phosphoribosyl-*N*-formylglycinamide (FGAR), was strongly depleted. Collectively, these observations suggest an unanticipated dependence of one-carbon metabolism on the oxPPP.

To confirm that this unexpected dependence of one-carbon metabolism is a direct consequence of G6PD loss, we re-expressed wild-type G6PD. This fully restored the knockout cells' NADPH/NADP ratio, malate and (iso)citrate levels, and dUMP levels (Fig. 5d,e and Supplementary Fig. 4a). Consistent with the maintained G6PD flux and NADPH/NADP ratio in PGD knockout cells, these cells did not accumulate dUMP (Supplementary Fig. 4b). To investigate whether these changes relate to the catalytic activity of G6PD, we expressed two G6PD point mutants: a dimerization interface mutant with markedly impaired catalytic activity (K403Q) and a catalytically dead mutant (K171Q) (Fig. 5d and Supplementary Fig. 4c). The K403Q mutant modestly restored the NADPH/NADP ratio and dUMP level in ΔG6PD cells, while the catalytically dead K171Q mutant had no effect (Fig. 5e,f). To investigate the sufficiency of G6PD catalytic activity in reversing the knockout phenotype, we re-expressed yeast G6PD. The yeast enzyme expression achieved lysate activities less than one-tenth of those normally

found in HCT116 cells (Supplementary Fig. 4d). Nevertheless, this partially normalized the NADPH/NADP ratio and dUMP levels (Supplementary Fig. 4e). Thus, rescue of the folate phenotype tracks with G6PD catalytic activity.

To explore why folate metabolism depends on G6PD, we fed ΔG6PD cells the soluble one-carbon donor formate. Formate provides a soluble source of 1C units and can normalize metabolite level changes due to 1C unit shortage. It cannot, however, compensate for impaired DHF reduction or blockade of folate-dependent biosynthetic enzymes. Formate did not mitigate the buildup of dUMP or AICAR in ΔG6PD cells (Supplementary Fig. 4f), suggesting that the defective metabolism was not related to an impaired supply of 1C units. To explore whether oxidative stress was the cause of the dysfunctional folate metabolism, we incubated wild-type cells with H_2O_2 . This decreased NADPH and the NADPH/NADP ratio but, unlike G6PD deletion, did not significantly increase NADP or dUMP levels (Supplementary Fig. 4g). To further explore the mechanism of the one-carbon deficiency in the ΔG6PD cells, we measured cellular folate species. In ΔG6PD cells, the levels of all 1C-loaded THF species dropped two to tenfold, with depletion of 5-methyl-THF, which is used for methionine biosynthesis, being particularly profound. While THF levels were only modestly affected, DHF increased 5- to 15-fold (Fig. 5c). DHF is a byproduct of thymidylate synthase and is converted to THF by DHFR using NADPH as the reductant. A simple explanation for these findings is impairment of DHFR activity in ΔG6PD cells.

We next investigated how G6PD deficiency may impair DHFR activity. Interestingly, DHFR protein levels and enzyme activity in lysates were comparable, if not higher, in both ΔG6PD clones (Fig. 5g and Supplementary Fig. 5a). We accordingly hypothesized that high NADP in ΔG6PD cells may inhibit DHFR. Consistent with this possibility, NADP impaired DHFR activity in cell lysates (Fig. 5g) and with recombinant human DHFR (Supplementary Fig. 5b).

We reasoned that mammalian DHFR might be particularly susceptible to product inhibition by NADP. To explore this, we engineered expression of both human and *E. coli* DHFR in ΔG6PD cells, to check for reversal of the one-carbon defects. Similar expression of both the human and *E. coli* enzyme was achieved on the basis of western blotting of their FLAG-tag (Supplementary Fig. 5c). On the basis of lysate activity assays, the *E. coli* enzyme was more active, and this was particularly true in the presence of high NADP (Supplementary Fig. 5d). Strikingly, the *E. coli*, but not human, enzyme largely reversed dUMP accumulation (Fig. 5h,i). This occurred without any rescue of oxidative stress sensitivity or increased folate-mediated NADPH production (Supplementary Fig. 5e,f). Thus, HCT116 cells require the oxPPP to maintain low NADP, which is necessary for DHFR activity and thereby folate homeostasis²⁴.

Generality of the dependence of folate metabolism on G6PD. We next explored the generality of the connection between G6PD, DHFR and folate metabolism across cultured cell lines. Analysis of cell lysates from 12 different cancer cell lines revealed that the activity of G6PD exceeded IDH1 and ME1 in each line, with the extent of IDH1 and ME1 activity variable (Supplementary Fig. 6a,b). We then examined the impact of G6PD gene knockout in five additional cell lines: transformed human embryonic kidney cells (HEK293T), triple negative breast cancer cells (MDA-468), pancreatic ductal adenocarcinoma cells (8988T), Ras-mutant lung adenocarcinoma cells (A549) and hepatocellular carcinoma cells (HepG2). Among these, A549 had the highest G6PD protein level and lysate activity and 8988T the lowest.

Cells were infected with lentivirus-expressing CRISPR enzymes, puromycin resistance markers and single guide RNA (sgRNA) targeting either a control sequence or G6PD gene. After puromycin selection, we obtained batch G6PD knockouts, with substantial G6PD depletion on the basis of immunoblotting (Supplementary Fig. 6c). Metabolomics analysis recapitulated the major metabolic

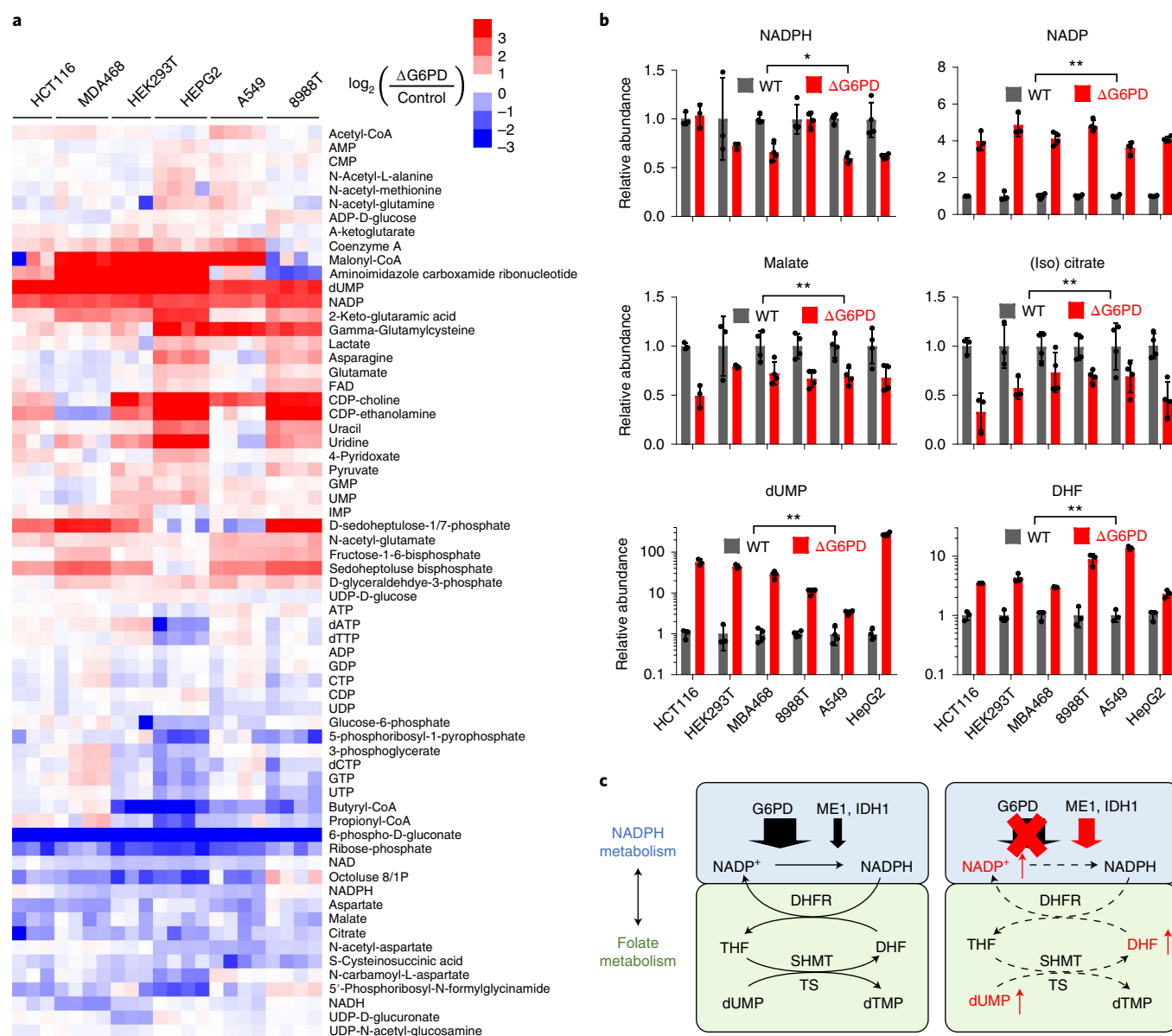


Fig. 6 | Across cell lines, G6PD knockout consistently causes folate deficiency. a, Heat map showing intracellular levels of water-soluble metabolites in G6PD deletion cells. For each cell line, three or four individual biological replicates are shown, normalized to respective WT cells. **b**, Relative levels of NADPH, NADP, malate, (iso)citrate, dUMP ($n = 3$ for HCT116 and HEK293T, $n = 4$ for others) and DHF ($n = 3$). Note that the dUMP and DHF panels are on a logarithmic y axis. **c**, Schematic: G6PD deletion leads to accumulation of NADP, DHF and dUMP. Data are mean \pm s.d. with n indicating the number of biological replicates. * $P < 0.05$ and ** $P < 0.01$ by two-tailed paired t -test assessing whether G6PD KO cell lines (as a group) differ from WT, with the geometric mean value for each cell type treated as one sample and $n = 6$, the number of cell lines (see Supplementary Table 3 for full statistical parameters). SHMT, serine hydroxymethyltransferase; TS, thymidylate synthase.

changes observed in clonal HCT116 deletion cell lines (Fig. 6a). 6-Phosphogluconate and ribose phosphate were strongly depleted (Fig. 6a), NADPH was nearly steady, NADP rose and malate and (iso)citrate were moderately decreased consistent with their consumption by compensatory ME1 and IDH1 flux. Most strikingly, dUMP and DHF increased greatly (Fig. 6b). Thus, G6PD is required to maintain NADP and folate homeostasis (Fig. 6c).

Discussion

NADPH's high-energy electrons drive reductive biosynthesis and redox defence. Here we systematically examined in HCT116 cells the impact of losing each or a combination of the major cytosolic NADPH production routes: oxPPP, IDH1 and ME1. While all three

are expressed and can contribute to NADPH production, we observe a hierarchy of importance. The oxPPP is the largest contributor to NADPH production, and is required to maintain a high NADPH/NADP ratio. IDH1 and ME1 appear to be 'backups', as (1) knocking them out did not impact growth in normoxia, yet either alone supported growth in the absence of oxPPP, with ME1 superior to IDH1 and (2) IDH1 or ME1 loss had minimal impact on sensitivity to oxidative stress. The primary role of the oxPPP seems to be shared across most cultured cancer cells, as (3) lysate enzyme activity measurements indicated that G6PD has higher NADPH production capacity than ME1 or IDH1 across 12 different cancer cell lines and (4) pooled G6PD knockouts of G6PD resulted in NADP buildup across five different cancer cell lines.

In vivo, the predominant cytosolic NADPH production pathway probably varies by tissue and cell type. Red blood cells depend on the oxPPP, as indicated by their sensitivity to hypomorphic G6PD alleles. This sensitivity may in part reflect their low expression of ME1 (despite strong expression of IDH1)²⁵. Lipogenic cells may depend more on IDH1 or malic enzyme^{14,26,27}. The importance of different NADPH production routes also presumably varies in response to environmental conditions. Intriguingly, in HCT116 cells, IDH1 was required for optimal growth in hypoxia, despite the presence of functional oxPPP, consistent with IDH1 being particularly important in low oxygen, perhaps for its role in reductive carboxylation^{28–30}. Understanding the tissue, cell type and environmental dependency of NADPH production routes is an important topic for ongoing study.

Are there additional biologically important cytosolic NADPH-producing enzymes? Previous ²H tracing studies in several transformed cell lines showed that 30–50% of cytosolic NADPH labelled from the oxPPP and only small amounts by ME1 or IDH1, suggesting a missing source for at least half of NADPH. In an effort to uncover the responsible enzyme, we carried out a CRISPR-based genetic screen in HCT116 cells engineered for sensitivity to loss of backup NADPH pathways by knockout of G6PD ± IDH1. The screen successfully identified ME1, the positive control, but no other NADPH-producing genes. While several hits were mitochondrial, they did not include any mitochondrial NADPH-producing enzymes, suggesting limited cross-talk between the cytosolic and mitochondrial NADPH pools. Consistent with the lack of other backups for making cytosolic NADPH, triple knockout of G6PD, ME1 and IDH1 was lethal. These findings align with recent evidence that the deficiency in NADPH labelling from the oxPPP, IDH1 and ME1 is due to flavin enzyme-catalysed H–D exchange with water, rather than an alternative route of NADP reduction¹⁵. Thus, although a substantial fraction of NADPH's redox-active hydrogen nucleus comes from H–D exchange with water, the high-energy electrons of cytosolic NADPH are almost exclusively from the oxPPP, ME1 and IDH1. It remains possible, however, that alternative pathways, either ALDH1L1 or yet to be characterized enzymes, are active in certain cell types or tissues.

In characterizing NADPH's H–D exchange process using D₂O labelling, we observed higher D₂O labelling in G6PD deletion cells¹⁵. The extent of such labelling depends on the degree of equilibration between NADPH and flavins. By decreasing the NADPH/NADP ratio, knockout of G6PD narrows the electrochemical potential difference between NADPH's and flavin's electrons, leading to more complete equilibration and higher D₂O labelling. In this manner, the extent of NADPH labelling from deuterated water serves as a surrogate for the NADP/NADPH ratio and rises with G6PD knockout.

Unexpectedly, a particularly sensitive cellular process to G6PD knockout proved to be folate metabolism. In ΔG6PD cells, impaired folate metabolism is evidenced by the accumulation of dUMP, GAR and AICAR, the substrates of folate-dependent reactions in thymidine and purine biosynthesis. It is reinforced by direct measurements of DHF accumulation and depletion of active 1C-loaded THF species. The most affected THF species is 5-methyl-THF, whose production requires NADPH not only to make THF but also to reduce methylene-THF to 5-methyl-THF. 5-Methyl-THF is a substrate for methionine synthase. In cell culture, this reaction is not important, due to methionine in media, but in vivo it maintains methylation potential.

The DHF accumulation suggests a mechanism in which G6PD knockout impairs DHFR activity. To provide evidence for this mechanism, we engineered expression of both human and *E. coli* DHFR, finding that only the latter could rescue the functional folate deficiency induced by G6PD loss. A probable mechanism by which G6PD might support human DHFR activity is maintenance of low

levels of NADP, a product inhibitor of DHFR³¹. It is possible that the dependence of mammalian folate metabolism on G6PD reflects evolutionary selection for tight DHFR–NADP binding, which turns off DHFR in response to a disfavoured NADPH/NADP ratio, thereby saving NADPH and/or decreasing nucleotide synthesis. We have previously shown that the antibiotic trimethoprim induces a cascade of enzyme inhibition in *E. coli*, starting with DHFR inhibition and propagating due to enzyme inhibition by accumulated DHF species³². Here, a cascade of inhibition seems to be triggered initially by NADP accumulation, and to propagate via DHFR inhibition and accumulation of DHF species.

This is the second connection between NADPH and folate metabolism to be uncovered in the past few years. The first involved folate-dependent NADPH production^{1,13}, which can occur via the ALDH1L1 enzyme in the cytosol or ALDH1L2 in the mitochondrion, which oxidizes 10-formyl-THF to make NADPH, THF and CO₂ (Supplementary Fig. 7). In HCT116 cells, ALDH1L1 and ALDH1L2 enzyme expression is minimal and therefore the folate pathway does not contribute substantial NADPH^{1,19,21,33}. While the biological role of cytosolic folate-mediated NADPH production remains unclear, ALDH1L2 promotes metastasis by enhancing tumour cell oxidative defence³⁴.

What is the biological rationale for the connections between NADPH and folate metabolism? Balanced quantities of NADPH and 1C units are needed for growth and proliferation. In cases where 1C unit supply exceeds NADPH availability, ALDH1L enzymes can burn a 1C unit to make NADPH³⁵. When this is insufficient to restore the NADPH/NADP ratio, high NADP impairs folate metabolism and thus nucleotide biosynthesis, halting proliferation to prioritize cell survival. In the cytosol, IDH1, ME1 and the oxPPP can all carry sufficient flux to meet the biosynthetic demand for NADPH. But only the oxPPP can do so while maintaining low NADP, rendering the oxPPP required for both redox and folate homeostasis.

Methods

Cell lines, growth conditions and reagents. HCT116 (CCL-247, lot no. 60506215) was purchased fresh from American Type Culture Collection (ATCC). HEK293T, MDA-MB-468, A549, HepG2, LnCap, MeWo, MDA-MB-231, U2OS, HT29, LN229 were from ATCC; 8988T, 8988S and KELLY cells were from DSMZ. Cell lines were cultured in 5% CO₂ at 37 °C using DMEM (CellGro, 10-017) supplemented with 10% foetal bovine serum (FBS) (F2442, Sigma-Aldrich) unless otherwise specified. Cas9 nickase and guide RNA expression plasmid pSpCasn(BB)-2A-Puro (48141), antiCRISPR v2 (52961) and GeCKOv2 in lentiCRISPR v2 (1000000048), and plasmid containing *E. coli* DHFR sequence (20214) were purchased from Addgene. Complementary DNA of G6PD (MHS6278-202826068) was from Dharmacon Inc. cDNA of human DHFR (RC200089) was purchased from OriGene Technologies. All primers were synthesized by IDT. Standard laboratory chemicals were from Sigma.

Generation of CRISPR knockouts. Clonal CRISPR knockouts were generated using the protocol of Ran and colleagues³³. Briefly, guide RNAs against exons of target genes (Supplementary Table 1) were cloned into a plasmid containing Cas9 nickase expression vector and puromycin-resistant genes. Cells were transiently transfected with plasmid targeting specific genes by using Lipofectamine 3000 (Life Technologies) and selected for 48 h with 2 µg ml⁻¹ puromycin. After selection, cells were allowed to grow to confluence before plating in 96 wells for single-cell selection. The single deletion cell lines lost puromycin resistance during single-cell cloning, which was conducted in the absence of puromycin. Double gene knockouts ΔG6PD/ΔIDH1 and ΔG6PD/ΔME1 were generated from knocking out IDH1 or ME1 in ΔG6PD background. ΔIDH1/ΔME1 was generated from knocking out ME1 in ΔIDH1 cell background. ΔG6PD knockout cells were grown in RPMI medium + 20% FBS during the recovery and single-cell selection period, as this yielded a greater fraction of clonal deletion cells than use of DMEM + 10% FBS. Functional gene deletion was confirmed by targeted genomic sequencing followed by western blotting.

Pooled CRISPR G6PD knockouts were generated using the protocol of Sanjana and colleagues³⁶. Briefly, sgRNA targeting intragenic control or G6PD gene was cloned into LentiCRISPR v2 vector plasmid using the BsmBI restriction endonuclease (NEB, R0580S). Lentivirus was prepared by transfecting a 10 cm plate of 293T cells with a mixture of 30 µl lipo3000 reagents, 6 µg prepared plasmid, 3 µg pMD2.G and 4.8 µg psPAX2 in 600 µl Opti-MEM. Medium containing pooled lentivirus was collected 2 days after transfection, filtered with a PES filter (0.22 µm,

Millipore) and stored in 1 ml aliquots at -80°C . HCT116, HEK293T, MBA468, 8988T, A549 and HepG2 cells were transduced with the control or G6PD targeting lentiviral constructs and $4\mu\text{l}^{-1}$ polybrene (Invitrogen). After 2 days of lentivirus transduction, cells were selected in $1-2\mu\text{g ml}^{-1}$ puromycin for 3 days. Cell stocks were made after first confluence and a new stock was used every 4 weeks. Functional gene deletion was confirmed by targeted genomic sequencing followed by western blotting.

CRISPR-based genetic screen. The CRISPR-based genetic screen was carried out using human GeCKOv2 in lentiCRISPR v2 (Addgene, 1000000048)³⁶. Two lentivirus libraries (A and B), each containing Cas9, puromycin resistance genes and sgRNA targeting 19,050 genes were generated by transfecting 15 cm plate of 293T cells with a mixture of 40 μl lipo3000 reagents, 10 μg GeCKOv2 library plasmid, 5 μg pMD2.G and 8 μg psPAX2 in 1000 μl Opti-MEM. Medium containing pooled lentivirus was collected 2 days after transfection, filtered with a PES filter (0.22 μm , Millipore) and stored in 5 ml aliquots at -80°C .

Two separate clones of HCT116 WT, ΔG6PD and $\Delta\text{G6PD}/\Delta\text{IDH1}$ cells were used. For each clone, two of 15 cm cultured plates with 15×10^6 cells each cultured in RPMI1640 medium supplemented with 10% FBS, were transduced with the above lentivirus libraries A and B, separately. After 2 days of lentivirus transduction, cells were selected in $1.5\mu\text{g ml}^{-1}$ puromycin for 2 days. Cells were then allowed to proliferate for ~ 15 generations in RPMI1640 medium supplemented with 10% FBS. A minimum of 15×10^6 cells were kept during every passaging to maintain the diversity of guide RNA libraries.

Genomic DNA of the first and last generation cells ($20-30 \times 10^6$ cells each) were extracted (Qiagen, 13343). SgRNA inserts were amplified by PCR, purified by gel filtration and sequenced on an Illumina HiSeq 2500 sequencer. Reads of each sgRNA were normalized to total reads within the sample. Results from two clones with same genetic background were pooled together to calculate Z-score between different genetic backgrounds (Supplementary Data).

Doxycycline-induced protein expression. Lentiviral Tet-On 3G Inducible Expression Systems (Clontech) was used for expression of WT, K171Q or K403Q human G6PD³⁷, yeast G6PD, human DHFR and *E. coli* DHFR, with synthetic DNA sequences containing a FLAG-tag. Genes of interest were cloned into pLVX-TRE3G vector through the NotI and MluI restriction sites.

Cells were first infected with lentivirus generated from pLVX-Tet3G (Clontech) and selected in $500\mu\text{g ml}^{-1}$ G418 for 3 days to establish Tet-On 3G transactivator protein expression. Then cells were infected with lentivirus generated from empty pLVX-TRE3G vector or pLVX-TRE3G containing human G6PD, human DHFR or *E. coli* DHFR. Cells were selected in $1.5\mu\text{g ml}^{-1}$ puromycin for 2 days to incorporate the gene of interest under the control of a TRE3G promoter. Protein expression was induced by incubating cells with $1\mu\text{g ml}^{-1}$ doxycycline.

Metabolite profiling. Cells were plated in six-well plates with DMEM supplemented with 10% dialysed FBS (Sigma). Fresh medium was supplied 24 h and 2 h before extraction. Cells were 60–90% confluent at the time of extraction. Media were removed by aspiration and metabolism was immediately quenched (without any washing steps) and metabolites extracted by adding $500\mu\text{l}$ -20°C 40:40:20 acetonitrile:methanol:water containing 0.5% formic acid and incubating on ice for 1–2 min before neutralizing with $44\mu\text{l}$ 15% ammonium bicarbonate. The cell extracts were then transferred to 1.5 ml tubes and stored at -20°C for 30 min. The extracts were cleared by centrifuging at $16,000g$ for 10 min and the supernatant was used for LC–MS analysis. LC–MS measurement was performed with a quadrupole orbitrap mass spectrometer (Q Exactive Plus, Thermo Fisher Scientific) operating in negative ion mode and coupled to hydrophilic interaction chromatography via electrospray ionization³⁸. The scan range was m/z 73 to 1,000. Liquid chromatography separation was achieved on a XBridge BEH Amide column (2.1 mm \times 150 mm, 2.5 μm particle size, 130 Å pore size; Waters) using a gradient of solvent A (20 mM ammonium acetate + 20 mM ammonium hydroxide in 95:5 water:acetonitrile, pH 9.45) and solvent B (acetonitrile). Flow rate was $150\mu\text{l min}^{-1}$. The gradient was: 0 min, 85% B; 2 min, 85% B; 3 min, 80% B; 5 min, 80% B; 6 min, 75% B; 7 min, 75% B; 8 min, 70% B; 9 min, 70% B; 10 min, 50% B; 12 min, 50% B; 13 min, 25% B; 16 min, 25% B; 18 min, 0% B; 23 min, 0% B; 24 min, 85% B; 30 min, 85% B. Peak identification and integration used MAVEN and ELMaven software, with compounds identified on the basis of exact mass and retention time match to commercial standards³⁹. After normalization to the average of wild-type samples, the resulting metabolite data were clustered using Cluster 3.0 software and plotted in Java Treeview.

Cell growth assay. Cell growth was measured using the CyQUANT proliferation assay kit according to manufacturer's instructions (Thermo). Briefly, cells were plated into a 96-well plate at 2,500–5,000 cells per well with $150\mu\text{l}$ DMEM supplemented with 10% FBS. Fluorescence intensity, which is proportional to the DNA content in the well, was read on consecutive days using a Synergy HT plate reader (BioTek Instruments). For hypoxic cell growth, the oxygen level was 0.5%. For oxidative stress cell growth, diamide or H_2O_2 was added during initial plating and cells were grown for the same duration thereafter.

In vitro enzyme activity assays. G6PD, IDH1, ME1 enzyme activity were determined in a diaphorase–resazurin coupled assay. The cytosolic fraction of cell lysates was collected using subcellular protein fractionation kit according to manufacturer's instruction (Thermo, 78840). The cytosolic fraction was added to assay buffer containing 50 mM Tris, pH 7.4, 5 mM MgCl_2 , 1 mM resazurin, 0.25 mM NADP, 0.1 U ml^{-1} diaphorase and 0.1 mg ml^{-1} BSA. Substrate (1 mM) (glucose-6-phosphate for G6PD, isocitrate for IDH1 and malate for ME1) was added to the above mixture to initiate reactions. Addition of glucose-6-phosphate can lead, via G6PD, to the production of 6-phosphogluconate and thus also NADPH production by PGD. Direct addition of 6-phosphogluconate to lysates resulted in $<10\%$ of the NADPH signal on glucose-6-phosphate addition, suggesting that the present assay largely measures G6PD activity.

To measure DHFR enzyme activity, whole-cell lysates were collected using CellLytic M (Sigma, C2978) according to manufacturer's instruction. Lysate was mixed with assay buffer containing 50 mM $\text{K}_2\text{HPO}_4/\text{KH}_2\text{PO}_4$, pH 7.4, 10 mM β -mercaptoethanol and 0.05 mM DHF and methotrexate or NADP as indicated. NADPH (0.1 mM) was added to the above mixture to initiate reactions. Activity was measured as the rate of decrease in NADPH fluorescence (in the absence of methotrexate) minus the decrease in the presence of methotrexate. Assay readout was by fluorescence for assays including diaphorase (530 nm excitation and 590 emission) and otherwise by absorption of NADPH at 340 nm, using a Synergy HT plate reader (BioTek Instruments). Enzyme activities were quantified from the slope of the fluorescence or absorption changes, and the absolute rate was calculated on the basis of the plateau which indicates full conversion of the limiting substrate. Measured enzyme activities were normalized to lysate protein concentration measured by BCA protein assay kit (Thermo, 23225).

Immunoblotting. Cells were cultured to 50–90% confluency in 6 cm plates. For whole-cell lysates, cells were washed with 4°C PBS once and lysed in RIPA buffer with phosphatase and protease inhibitors (Roche). Subcellular lysates were collected using subcellular protein fractionation kit according to manufacturer's instruction (Thermo, 78840). Lysates were cleared by 10 min centrifugation at $16,000g$ at 4°C . Samples were resolved by SDS–PAGE on precast gels (Bio-Rad) and transferred to a nitrocellulose membrane using the Trans-Blot Turbo system (Bio-Rad). Primary antibodies and horseradish peroxidase-conjugated secondary antibodies were used according to manufacturer's directions. The ChemiDoc XRS+ system was used for image acquisition. Antibodies were used according to their manufacturer's directions. Antibodies to β -actin (5125) and FLAG-tag (2368) were obtained from Cell Signaling Technologies. Antibodies to G6PD (ab993), ME1 (ab97445), IDH1 (EP12296) and PGD (EP6565) were obtained from Abcam Inc. Antibodies to DHFR (377091) and TS (390945) were obtained from Santa Cruz Biotechnology. Uncropped blots are provided in the Supplementary Information.

Isotope labelling. The following isotopic tracers were purchased from the indicated sources: D_2O , [^{13}C]glucose, [^{13}C]glutamine, [2,3,4,4- ^2H]glutamine (Cambridge Isotope Laboratories); [^3H]myristic acid (Sigma); [3- ^2H]glucose (Omicron Biochemicals). Isotope-labelled glucose, glutamine or D_2O medium were prepared from phenol red-, glucose-, glutamine-, sodium pyruvate-, sodium bicarbonate-free DMEM powder (Cellgro) supplemented with 3.7 g l^{-1} sodium bicarbonate, 25 mM glucose, 4 mM glutamine and 10% dialysed FBS.

NADPH measurement and redox-active hydrogen calculation. Cells were plated in six-well plates with DMEM supplemented with 10% dialysed FBS (Sigma) for 24 h. Cells were fed with [3- ^2H]glucose, [2,3,4,4- ^2H]glutamine or D_2O medium for 2 h. NADPH and NADP labelling was measured as described in the Section 'Metabolite profiling', except in the LC–MS analysis, an additional scan event with m/z window ranging from 650 to 760 was included.

The mass difference between $^{13}\text{C}_1$ and $^1\text{H}_1$ NADPH and NADP cannot be resolved using the Q Exactive Plus. Therefore, the natural ^{13}C abundance was corrected from the raw data. Over 2 h labelling duration, NADPH became M + 1 and M + 2 labelled, while NADP was only M + 1 labelled. The labelling of the redox-active hydrogen of NADPH ([Active-H]) was determined using the following equation:

$$[\text{NADP}] \times [\text{Active} - \text{H}] = [\text{NADPH}]$$

$$\begin{bmatrix} \text{M} + 0 & 0 \\ \text{M} + 1 & \text{M} + 0 \\ 0 & \text{M} + 1 \end{bmatrix} \times \begin{bmatrix} x \\ 1-x \end{bmatrix} = \begin{bmatrix} \text{M} + 0 \\ \text{M} + 1 \\ \text{M} + 2 \end{bmatrix} \quad (1)$$

Correction for solvent exchange on Active-H labelling was performed according to previous literature¹⁵. In brief, the extent of the solvent exchange fraction can be quantified by dividing the Active-H labelling fraction from D_2O to media D_2O percentage. Then Active-H labelling from [2,3,4,4- ^2H]glutamine or [3- ^2H]glucose can be corrected by normalizing to the un-exchanged fraction or 1 – solvent exchange fraction.

$$\text{Active-H}_{\text{corrected}} = \text{Active-H}_{\text{measured}} \left(1 - \frac{\text{Active-H}_{\text{D}_2\text{O}}}{\text{D}_2\text{O percentage}} \right) \quad (2)$$

It should be noted that, the solvent exchange correction may be overestimated in cells that mainly use ME1 and IDH1 to make NADPH, because D₂O not only labels NADPH directly through flavin-dependent proton exchange, but also labels malate and isocitrate and thereby indirectly labels NADPH.

Folate measurements. Folate species were measured according to previous literature¹⁰. In short, folates were extracted from cultured cells with 50:50 H₂O:MeOH containing 25 mM sodium ascorbate and 25 mM NH₄OAc at pH 7. Cell extracts were heated to 60°C for 5 min to fully denature proteins and were cleared by centrifugation at 16,000g for 5 min at 4°C. Supernatants were dried under N₂ flow and resuspended in 450 µl potassium phosphate buffer (50 mM with 30 mM ascorbic acid and 0.5% 2-mercaptoethanol at pH 7) and 25 µl rat serum for 37°C incubation for 2 h. To clean up samples before LC-MS, Bond Elut-PH SPE columns (Agilent) were conditioned with 1 ml MeOH and then with 1 ml wash buffer (30 mM ascorbic acid in 25 mM NH₄OAc buffer at pH 4.0). After adjusting the samples to pH 4 with 7 µl of 40% formic acid solution at 4°C, the samples were loaded onto the conditioned SPE columns, washed with 1 ml wash buffer and subsequently eluted with 400 µl elution buffer (50:50 H₂O:MeOH containing 0.5% 2-mercaptoethanol and 25 mM NH₄OAc at pH 7). The eluate was dried down under N₂ flow, resuspended into high pressure liquid chromatography water, centrifuged to remove possible precipitate, kept at 4°C in an autosampler and analysed by reverse phase LC-MS within 12 h to minimize degradation.

Fatty acid synthesis measurements. Cells were cultured in [U-¹³C]glucose DMEM medium supplemented with 10% dialysed FBS for five generations. Then the cells were plated in a six-well plate for an additional 2 days with [U-¹³C]glucose medium. Metabolism was quenched and cells were extracted using 90:10 MeOH:water containing 0.3 M KOH and 3.9 nmol [U-²H]myristic acid internal standard. The extraction mixture was transferred into a 4 ml glass vial and incubated for 1 h at 80°C for saponification. The saponified fatty acids were acidified with 100 µl formic acid and extracted with 1 ml hexane into a 2 ml sample loading vial. Hexane was dried under N₂ and the resulting fatty acids were re-dissolved into 50:50 MeOH:isopropanol for LC-MS analysis. LC-MS analysis was achieved as described previously³⁸. Briefly, MS analysis was conducted on an Exactive orbitrap mass spectrometer (Thermo Fisher Scientific) operating in negative ion mode. Liquid chromatography separation was on reversed phase ion pairing chromatography on a Luna C8 column (150 × 2.0 mm², 3 µm particle size, 100 Å pore size; Phenomenex) with a gradient of solvent A (10 mM tributylamine + 15 mM acetic acid in 97:3 H₂O:MeOH, pH 4.5) and solvent B (MeOH).

Fatty acid content per cell volume was calculated by first normalizing measured fatty acid intensity to the internal standard and then dividing by the measured packed cell volume (PCV). Fatty acid de novo synthesis fraction was the sum of specific ¹³C labelling fractions as described in Supplementary Table 2. The ¹³C₂ (that is M2) species were not included in the de novo synthesis fraction for C18 fatty acids, as we observed a substantial M2 peak consistent with elongation from pre-existing C16 species (Supplementary Fig. 3).

NADPH consumption per fatty acid species was the product of the de novo synthesis fraction and the number of NADPH used to synthesize that fatty acid species. Total NADPH consumption for fatty acid is the sum of NADPH consumption for six fatty acid species (Supplementary Table 2), which account for most of the fatty acid content in cultured cells. NADPH consumption rate for fatty acid synthesis was calculated as total NADPH consumed for fatty acid per cell volume multiplied by the cell proliferation rate. Cell proliferation rate is equal to ln(2) divided by doubling time.

Malic enzyme flux calculation. Total malic enzyme flux, including all isozymes, was quantified on the basis of M + 3 pyruvate labelling from [U-¹³C]glutamine relative to glycolysis flux as described previously¹⁴. Forward flux of TCA cycle from [U-¹³C]glutamine results in M + 4 malate. Turning TCA cycle or reductive carboxylation of glutamine coupled to citrate lyase can produce M + 3 malate. While M + 4 malate produces M + 3 pyruvate, isotopologues of M + 3 malate produce half M + 2 and half M + 3 pyruvate. Spent media after 24 h of cell cultures were measured by YSI 2900 instrument to obtain the lactic secretion flux, which is approximate to the glycolysis flux.

$$\frac{\text{Total malic enzyme flux}}{\text{Glycolysis flux}} = \frac{\text{Pyruvate M+3 fraction}}{\text{Malate M+4 fraction} + 0.5 \times \text{Malate M+3 fraction}} \quad (3)$$

CO₂ release and oxPPP flux. The absolute oxPPP flux was quantified using ¹⁴CO₂ release from [1-¹⁴C]glucose and [6-¹⁴C]glucose as previously described¹⁵. Briefly, cells were grown in 12.5 cm² tissue culture flasks with pH 7.4 DMEM containing 6 g l⁻¹ HEPES (D9805 US Biological) and low bicarbonate (0.74 g l⁻¹). [1-¹⁴C] Glucose or [6-¹⁴C]glucose (0.5 µCi ml⁻¹) was added to the medium and the flask was sealed with a rubber stopper with a centre well (Kimble Chase) containing thick pieces of filter paper saturated with 150 µl 10 M KOH. Cells were incubated

for 24 h. Metabolism was quenched and CO₂ was released by injecting 1 ml 3 M acetic acid through the stopper. The flask was incubated at 37°C for 1 h to allow full absorption of released CO₂ to the filter paper. The filter paper and KOH solution in the centre well was transferred into a scintillation vial containing 10 ml liquid scintillation cocktail (PerkinElmer). Water (100 µl) was used to rinse the well and was combined with the same scintillation vial for scintillation counting. The signal was corrected for the percentage of radioactive tracer in the medium. OxPPP flux was calculated as follows:

$$\text{oxPPP flux (mM h}^{-1}\text{)} = \frac{{}^{14}\text{CO}_2 \text{ (nmol)}}{\text{PCV (}\mu\text{l cell)} \times \text{labelling time (h)}} \times \frac{\text{Total glucose (nmol)}}{{}^{14}\text{C-glucose (nmol)}} \quad (4)$$

Statistics and reproducibility. Sample sizes, error bars and *P* values are defined in each figure legend. For immunoblotting results or DNA sequencing results, we show representative data from multiple replicates: Fig. 1b (*n* = 3), Supplementary Fig. 1a (*n* = 3), Supplementary Fig. 2e (*n* = 2), Supplementary Fig. 4c (*n* = 2), Supplementary Fig. 5a (*n* = 2), Supplementary Fig. 5c (*n* = 2), Supplementary Fig. 6c (*n* = 2). Sample sizes, centre values, error bars and statistical test methods are specified in the figure legends. All statistical calculations were performed using the software package GraphPad Prism v.7.03.

Reporting Summary. Further information on research design is available in the Nature Research Reporting Summary linked to this article.

Data availability

Source data used to generate Fig. 2a–c and Supplementary Fig. 2b–d are provided as Supplementary Data 1. Uncropped versions of blots are provided in Supplementary Figs. 8–13. Other data that support the findings of this study are available from the authors upon request. Matlab code used for matrix deconvolution for NADPH redox hydride is provided as Supplementary Note 1. R code and R package used for natural abundance correction are publicly available from GitHub (<https://github.com/XiaoyangSu/Isotope-Natural-Abundance-Correction> and <https://github.com/lparsons/accucor>)⁴¹.

Received: 26 May 2018; Accepted: 5 February 2019;

Published online: 11 March 2019

References

- Lewis, C. A. et al. Tracing compartmentalized NADPH metabolism in the cytosol and mitochondria of mammalian cells. *Mol. Cell* **55**, 253–263 (2014).
- Lunt, S. Y. & Heiden, M. G. V. Aerobic glycolysis: meeting the metabolic requirements of cell proliferation. *Annu. Rev. Cell Dev. Biol.* **27**, 441–464 (2011).
- Jiang, P. et al. p53 regulates biosynthesis through direct inactivation of glucose-6-phosphate dehydrogenase. *Nat. Cell Biol.* **13**, 310–316 (2011).
- Jiang, P., Du, W., Mancuso, A., Wellen, K. E. & Yang, X. Reciprocal regulation of p53 and malic enzymes modulates metabolism and senescence. *Nature* **493**, 689–693 (2013).
- Cappellini, M. & Fiorelli, G. Glucose-6-phosphate dehydrogenase deficiency. *Lancet* **371**, 64–74 (2008).
- Howes, R. E. et al. Spatial distribution of G6PD deficiency variants across malaria-endemic regions. *Malar. J.* **12**, 418 (2013).
- Al-Dwairi, A., Pabona, J. M. P., Simmen, R. C. M. & Simmen, F. A. Cytosolic malic enzyme 1 (ME1) mediates high fat diet-induced adiposity, endocrine profile, and gastrointestinal tract proliferation-associated biomarkers in male mice. *PLoS ONE* **7**, e46716 (2012).
- Itsumi, M. et al. Idh1 protects murine hepatocytes from endotoxin-induced oxidative stress by regulating the intracellular NADP⁺/NADPH ratio. *Cell Death Differ.* **22**, 1837–1845 (2015).
- Nicol, C. J., Zielinski, J., Tsui, L.-C. & Wells, P. G. An embryoprotective role for glucose-6-phosphate dehydrogenase in developmental oxidative stress and chemical teratogenesis. *FASEB J.* **14**, 111–127 (2000).
- Buescher, J. M. et al. A roadmap for interpreting ¹³C metabolite labeling patterns from cells. *Curr. Opin. Biotechnol.* **34**, 189–201 (2015).
- Katz, J. & Rognstad, R. The labeling of pentose phosphate from glucose-¹⁴C and estimation of the rates of transaldolase, transketolase, the contribution of the pentose cycle, and ribose phosphate synthesis. *Biochemistry* **6**, 2227–2247 (1967).
- Metallo, C. M., Walther, J. L. & Stephanopoulos, G. Evaluation of ¹³C isotopic tracers for metabolic flux analysis in mammalian cells. *J. Biotechnol.* **144**, 167–174 (2009).
- Fan, J. et al. Quantitative flux analysis reveals folate-dependent NADPH production. *Nature* **510**, 298–302 (2014).

14. Liu, L. et al. Malic enzyme tracers reveal hypoxia-induced switch in adipocyte NADPH pathway usage. *Nat. Chem. Biol.* **12**, 345–352 (2016).
15. Zhang, Z., Chen, L., Liu, L., Su, X. & Rabinowitz, J. D. Chemical basis for deuterium labeling of fat and NADPH. *J. Am. Chem. Soc.* **139**, 14368–14371 (2017).
16. Shreve, D. S. & Levy, H. R. Kinetic mechanism of glucose-6-phosphate dehydrogenase from the lactating rat mammary gland. Implications for regulation. *J. Biol. Chem.* **255**, 2670–2677 (1980).
17. Ducker, G. S. & Rabinowitz, J. D. One-carbon metabolism in health and disease. *Cell Metab.* **25**, 27–42 (2017).
18. Locasale, J. W. Serine, glycine and one-carbon units: cancer metabolism in full circle. *Nat. Rev. Cancer* **13**, 572–583 (2013).
19. Tibbetts, A. S. & Appling, D. R. Compartmentalization of mammalian folate-mediated one-carbon metabolism. *Annu. Rev. Nutr.* **30**, 57–81 (2010).
20. Yang, M. & Voutsden, K. H. Serine and one-carbon metabolism in cancer. *Nat. Rev. Cancer* **16**, 650–662 (2016).
21. Ducker, G. S. et al. Reversal of cytosolic one-carbon flux compensates for loss of the mitochondrial folate pathway. *Cell Metab.* **23**, 1140–1153 (2016).
22. Ye, J. et al. Serine catabolism regulates mitochondrial redox control during hypoxia. *Cancer Discov.* **4**, 1406–1417 (2014).
23. Ran, F. A. et al. Genome engineering using the CRISPR-Cas9 system. *Nat. Protoc.* **8**, 2281–2308 (2013).
24. Appleman, J. R. et al. Unusual transient- and steady-state kinetic behavior is predicted by the kinetic scheme operational for recombinant human dihydrofolate reductase. *J. Biol. Chem.* **265**, 2740–2748 (1990).
25. Nemkov, T. et al. Metabolism of citrate and other carboxylic acids in erythrocytes as a function of oxygen saturation and refrigerated storage. *Front. Med. (Lausanne)* **4**, 175 (2017).
26. Flatt, J. P. & Ball, E. G. Studies on the metabolism of adipose tissue XV. An evaluation of the major pathways of glucose catabolism as influenced by insulin and epinephrine. *J. Biol. Chem.* **239**, 675–685 (1964).
27. Koh, H.-J. et al. Cytosolic NADP⁺-dependent isocitrate dehydrogenase plays a key role in lipid metabolism. *J. Biol. Chem.* **279**, 39968–39974 (2004).
28. Jiang, L. et al. Reductive carboxylation supports redox homeostasis during anchorage-independent growth. *Nature* **532**, 255–258 (2016).
29. Metallo, C. M. et al. Reductive glutamine metabolism by IDH1 mediates lipogenesis under hypoxia. *Nature* **481**, 380 (2011).
30. Wise, D. R. et al. Hypoxia promotes isocitrate dehydrogenase-dependent carboxylation of α -ketoglutarate to citrate to support cell growth and viability. *Proc. Natl Acad. Sci. USA* **108**, 19611–19616 (2011).
31. Liu, C. T. et al. Functional significance of evolving protein sequence in dihydrofolate reductase from bacteria to humans. *Proc. Natl Acad. Sci. USA* **110**, 10159–10164 (2013).
32. Kwon, Y. K. et al. A domino effect in antifolate drug action in *Escherichia coli*. *Nat. Chem. Biol.* **4**, 602–608 (2008).
33. Field, M. S., Kamynina, E., Watkins, D., Rosenblatt, D. S. & Stover, P. J. Human mutations in methylenetetrahydrofolate dehydrogenase 1 impair nuclear de novo thymidylate biosynthesis. *Proc. Natl Acad. Sci. USA* **112**, 400–405 (2015).
34. Piskounova, E. et al. Oxidative stress inhibits distant metastasis by human melanoma cells. *Nature* **527**, 186–191 (2015).
35. Zheng, Y. et al. Mitochondrial one-carbon pathway supports cytosolic folate integrity in cancer cells. *Cell* **175**, 1546–1560.e17 (2018).
36. Sanjana, N. E., Shalem, O. & Zhang, F. Improved vectors and genome-wide libraries for CRISPR screening. *Nat. Methods* **11**, 783–784 (2014).
37. Wang, Y.-P. et al. Regulation of G6PD acetylation by SIRT2 and KAT9 modulates NADPH homeostasis and cell survival during oxidative stress. *EMBO J.* **33**, 1304–1320 (2014).
38. Hui, S. et al. Glucose feeds the TCA cycle via circulating lactate. *Nature* **551**, 115–118 (2017).
39. Melamud, E., Vastag, L. & Rabinowitz, J. D. Metabolomic analysis and visualization engine for LC–MS data. *Anal. Chem.* **82**, 9818–9826 (2010).
40. Chen, L., Ducker, G. S., Lu, W., Teng, X. & Rabinowitz, J. D. An LC-MS chemical derivatization method for the measurement of five different one-carbon states of cellular tetrahydrofolate. *Anal. Bioanal. Chem.* **409**, 5955–5964 (2017).
41. Su, X., Lu, W. & Rabinowitz, J. D. Metabolite spectral accuracy on orbitraps. *Anal. Chem.* **89**, 5940–5948 (2017).

Acknowledgements

We thank G. Ducker, J. Ghergurovich and X. Teng for scientific discussion and help. This work was supported by funding from the US National Institutes of Health (grant nos. R01CA163591, P30CA072720, DP1DK113643, P30DK019525, R01DK107667 and R01DK114103) and Department of Energy (grant nos. DE-SC0018420 and DE-SC0018260).

Author contributions

L.C. and J.D.R. came up with the general approach. L.C., Z.Z. and H.D.Z. generated and characterized different cell lines used in this studies. L.C., A.H., M.M., Z.A. and J.D.R. designed and performed CRISPR libraries screening. L.C. and Z.Z. designed and performed isotope tracing studies. L.C. performed metabolomics studies. L.C. and J.D.R. wrote the paper with help from all authors.

Competing interests

J.D.R. is a founder of Raze Therapeutics and advisor to L.E.A.F. Pharmaceuticals. J.D.R. is a co-inventor on patent application owned by Princeton University covering diagnostics and therapeutics related to NADPH production by the 10-formyl-THF pathway (US20170000769).

Additional information

Supplementary information is available for this paper at <https://doi.org/10.1038/s42255-019-0043-x>.

Reprints and permissions information is available at www.nature.com/reprints.

Correspondence and requests for materials should be addressed to J.D.R.

Publisher's note: Springer Nature remains neutral with regard to jurisdictional claims in published maps and institutional affiliations.

© The Author(s), under exclusive licence to Springer Nature Limited 2019

Reporting Summary

Nature Research wishes to improve the reproducibility of the work that we publish. This form provides structure for consistency and transparency in reporting. For further information on Nature Research policies, see [Authors & Referees](#) and the [Editorial Policy Checklist](#).

Statistical parameters

When statistical analyses are reported, confirm that the following items are present in the relevant location (e.g. figure legend, table legend, main text, or Methods section).

n/a Confirmed

- ☐ ☒ The exact sample size (n) for each experimental group/condition, given as a discrete number and unit of measurement
- ☐ ☒ An indication of whether measurements were taken from distinct samples or whether the same sample was measured repeatedly
- ☐ ☒ The statistical test(s) used AND whether they are one- or two-sided
Only common tests should be described solely by name; describe more complex techniques in the Methods section.
- ☒ ☐ A description of all covariates tested
- ☐ ☒ A description of any assumptions or corrections, such as tests of normality and adjustment for multiple comparisons
- ☐ ☒ A full description of the statistics including central tendency (e.g. means) or other basic estimates (e.g. regression coefficient) AND variation (e.g. standard deviation) or associated estimates of uncertainty (e.g. confidence intervals)
- ☐ ☒ For null hypothesis testing, the test statistic (e.g. F , t , r) with confidence intervals, effect sizes, degrees of freedom and P value noted
Give P values as exact values whenever suitable.
- ☒ ☐ For Bayesian analysis, information on the choice of priors and Markov chain Monte Carlo settings
- ☒ ☐ For hierarchical and complex designs, identification of the appropriate level for tests and full reporting of outcomes
- ☒ ☐ Estimates of effect sizes (e.g. Cohen's d , Pearson's r), indicating how they were calculated
- ☐ ☒ Clearly defined error bars
State explicitly what error bars represent (e.g. SD, SE, CI)

Our web collection on [statistics for biologists](#) may be useful.

Software and code

Policy information about [availability of computer code](#)

Data collection

BioTek Gen 5.1.11 was used to collect fluorescent and absorption data for enzyme assay.
HiSeq 2500 was used to collect DNA sequencing data for CRISPR screen.

Data analysis

Prism 7.03 was used to data plotting and statistical analysis.
Matlab code used for matrix deconvolution for NADPH redox hydride is provided.
Maven (build 682) and ElMaven (0.2.4) used for metabolomics data analysis.
Cluster 3.0 and Java Treeview used for plotting heat map.
R code and R package were used for natural abundance correction are publicly available from GitHub (<https://github.com/XiaoyangSu/Isotope-Natural-Abundance-Correction> and <https://github.com/lparsons/accucor>).

For manuscripts utilizing custom algorithms or software that are central to the research but not yet described in published literature, software must be made available to editors/reviewers upon request. We strongly encourage code deposition in a community repository (e.g. GitHub). See the Nature Research [guidelines for submitting code & software](#) for further information.

Data

Policy information about [availability of data](#)

All manuscripts must include a [data availability statement](#). This statement should provide the following information, where applicable:

- Accession codes, unique identifiers, or web links for publicly available datasets
- A list of figures that have associated raw data
- A description of any restrictions on data availability

Source Data used to generate Figs 2a-c and Supplementary Figs 2b-d are provided as Supplementary Data 1. Uncropped versions of blots are provided in Supplementary Figures 8-13. Other data that support the findings of this study are available from the authors upon request.

Field-specific reporting

Please select the best fit for your research. If you are not sure, read the appropriate sections before making your selection.

☒ Life sciences ☐ Behavioural & social sciences ☐ Ecological, evolutionary & environmental sciences

For a reference copy of the document with all sections, see [nature.com/authors/policies/ReportingSummary-flat.pdf](https://www.nature.com/authors/policies/ReportingSummary-flat.pdf)

Life sciences study design

All studies must disclose on these points even when the disclosure is negative.

Sample size	Statistical methods were not used to predetermine sample size. Sample size was determined by experimental feasibility and sample availability to demonstrate certain results.
Data exclusions	No data were excluded from the analyses.
Replication	Biological replications and statistics were indicated in the legends. All attempts at replication were successful based on replications on different days showing comparable significance level for biological comparison.
Randomization	Samples were allocated into experimental groups by the confirmed genetic modification of the cell line (e.g. CRISPR-Cas9 deletion, doxycycline-induced protein re-expression) and/or culturing conditions (e.g. isotope tracing). This design does not allow for randomization, as the origin of samples is critical. However, whenever possible samples were analyzed in a randomized order (i.e. when run on liquid-chromatography mass spectrometry).
Blinding	The researchers were not blinded during data collection and/or analysis as this study did not involve animals or human research participants.

Reporting for specific materials, systems and methods

Materials & experimental systems

n/a	Involved in the study
<input checked="" type="checkbox"/>	<input type="checkbox"/> Unique biological materials
<input type="checkbox"/>	<input checked="" type="checkbox"/> Antibodies
<input type="checkbox"/>	<input checked="" type="checkbox"/> Eukaryotic cell lines
<input checked="" type="checkbox"/>	<input type="checkbox"/> Palaeontology
<input checked="" type="checkbox"/>	<input type="checkbox"/> Animals and other organisms
<input checked="" type="checkbox"/>	<input type="checkbox"/> Human research participants

Methods

n/a	Involved in the study
<input checked="" type="checkbox"/>	<input type="checkbox"/> ChIP-seq
<input checked="" type="checkbox"/>	<input type="checkbox"/> Flow cytometry
<input checked="" type="checkbox"/>	<input type="checkbox"/> MRI-based neuroimaging

Antibodies

Antibodies used

Antibodies were used in according to the manufacturer's directions.
 Anti-Rabbit β -Actin (13E5) Cell Signaling Technologies #5125 (1:20000)
 Anti-Rabbit DYKDDDDK Tag Antibody (Binds to same epitope as Sigma's Anti-FLAG[®] M2 Antibody) Cell Signaling Technologies #2368 (1:2500)
 Anti-Rabbit G6PD Abcam (ab993) (1:2500)
 Anti-Rabbit ME1 Abcam (ab97445) (1:2500)
 Anti-Rabbit IDH1 (EPR12296) Abcam (1:2500)
 Anti-Rabbit PGD (EPR6565) Abcam (1:2500)

Validation

Anti-Mouse DHFR Antibody (A-9): Santa Cruz (377091) (1:100)
 Anti-Mouse TS Antibody (C-5) Santa Cruz (390945) (1:100)

Antibodies were validated by the providers with validation and antibody profiles in the links. In addition, antibodies against G6PD, IDH1, ME1 and PGD used in this study were cross-validated in this study by the loss of the specific band in CRISPR/Cas9 knockout cell lines.

Abcam antibodies:

Anti-G6PD (ab993)

<https://www.abcam.com/glucose-6-phosphate-dehydrogenase-antibody-ab993.html>

Also validated by whole cell lysates from CRISPR/Cas9 knockout cells.

Anti-ME1 (ab97445)

<https://www.abcam.com/me1-antibody-ab97445.html>

Also validated by cell cytosolic fraction lysates from CRISPR/Cas9 knockout cells.

Anti-IDH1 (EPR12296)

<https://www.abcam.com/isocitrate-dehydrogenase-antibody-epr12296-ab172964.html>

Also validated by both whole cell and cytosolic fraction lysates from CRISPR/Cas9 knockout cells.

Anti-PGD (EPR6565)

<https://www.abcam.com/pgd-antibody-epr6565-ab129199.html>

Also validated by whole cell lysates from CRISPR/Cas9 knockout cells.

Cell Signaling antibodies:

Anti-Flag-tag (2368)

<https://www.cellsignal.com/products/primary-antibodies/dykdddk-tag-antibody-binds-to-same-epitope-as-sigma-s-anti-flag-m2-antibody/2368>

Also validated by doxycycline-induction of Flag-tag protein re-expression.

Anti- β -actin (5125)

<https://www.cellsignal.com/products/antibody-conjugates/b-actin-13e5-rabbit-mab-hrp-conjugate/5125>

Santa Cruz antibodies:

Anti-DHFR (377091)

<https://www.scbt.com/scbt/product/dhfr-antibody-a-9>

Anti-TS (390945)

<https://www.scbt.com/scbt/product/ts-antibody-c-5>

Eukaryotic cell lines

Policy information about [cell lines](#)

Cell line source(s)

HCT116 (CCL-247, lot# 60506215) was purchased fresh from ATCC (Manassas, VA). HEK293T, MDA-MB-468, A549, HepG2, LnCap, MeWo, MDA-MB-231, U2OS, HT29, LN229 were from ATCC; 8988T, 8988S and KELLY cells were from DSMZ (Braunschweig, Germany).

Authentication

Cell lines used in this study have not been authenticated after purchasing from vendors. CRISPR knockout cells were authenticated by immunoblotting of targeted proteins and Sanger sequencing of modification region of targeted genes.

Mycoplasma contamination

All cells used have been tested negative for mycoplasma contamination.

Commonly misidentified lines (See [ICLAC](#) register)

No such cell lines were used.